

MULTIMODAL SENSING FOR ROBOT-ASSISTED SUB-TISSUE FEATURE DETECTION IN PHYSIOTHERAPY PALPATION

Tian-Ao Ren^{1,*}, Jorge Garcia¹, Seongheon Hong¹,
Jared Grinberg², Hojung Choi¹, Julia Di¹, Hao Li¹, Dmitry Grinberg², Mark R. Cutkosky^{1,*}

¹Stanford University, Stanford, CA

²Symbiokinetics Inc, Palo Alto, CA

ABSTRACT

Robotic palpation relies on force sensing, but force signals in soft-tissue environments are variable and cannot reliably reveal subtle subsurface features. We present a compact multimodal sensor that integrates high-resolution vision-based tactile imaging with a 6-axis force–torque sensor. In experiments on silicone phantoms with diverse subsurface tendon geometries, force signals alone frequently produce ambiguous responses, while tactile images reveal clear structural differences in presence, diameter, depth, crossings, and multiplicity. Yet accurate force tracking remains essential for maintaining safe, consistent contact during physiotherapeutic interaction. Preliminary results show that combining tactile and force modalities enables robust subsurface feature detection and controlled robotic palpation.

Keywords: Tactile sensing, force sensing, multimodal sensing, medical palpation, tissue manipulation

1. INTRODUCTION

A foundational diagnostic skill, palpation enables clinical practitioners to assess tissue stiffness, localize tendons, and identify abnormalities beneath soft tissue [1, 2]. Clinicians naturally integrate applied force with tactile perception, adjusting pressure while interpreting local deformation cues. Replicating this capability in robotic systems remains challenging. Traditional robotic palpation methods rely on force sensing (e.g. [3, 4]), but force signals can be difficult to interpret in soft-tissue environments.

In the present context, we are particularly interested in physiotherapy applications (e.g. acupressure [5–7]) which combine palpation with large, targeted applications of pressure—necessitating both accurate force control and robust hardware that can apply and withstand forces of 100 N routinely.

The ambiguity arising from force/torque contact data is evident even in controlled settings: as shown later, sliding across a silicone phantom while pressing firmly can produce substantially

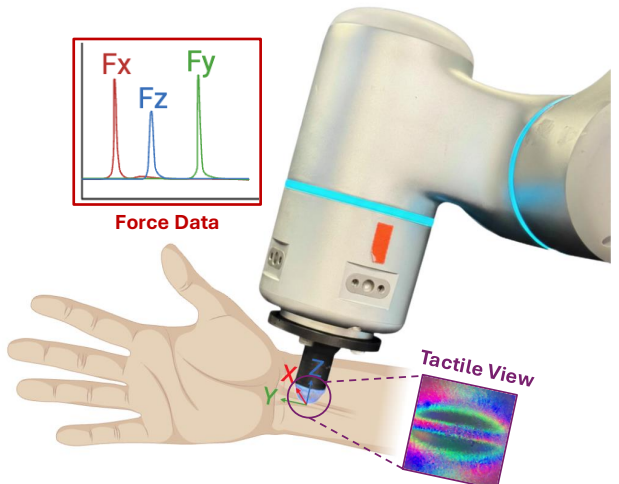


FIGURE 1: The PhysioVisionFT (PVFT) concept: a force/torque sensor captures (F_x , F_y , F_z) contact force data; a camera captures high-resolution visuotactile images, enabling safe and controlled contact for physiotherapy.

different force profiles depending on the local geometry as well as whether there are subsurface features. Variations in force profiles can also arise from fine-scale sub-surface features, especially when geometry differences involve small height changes, lateral variations, crossings, or tendon multiplicity [8].

Vision-based tactile sensors have become popular for providing high-resolution deformation measurements (e.g. [9–14]). However, these are often too compliant or fragile for physiotherapy-scale interactions, where contact forces commonly exceed tens of newtons. Moreover, the estimation of contact forces from deflection patterns can be challenging, especially when in contact with soft tissues that contain subsurface features.

To address these gaps, we present PhysioVisionFT (PVFT), a compact, mechanically robust multimodal sensor that integrates a high-resolution fisheye tactile dome with a 6-axis CoinFT

*Corresponding author: tiaao@stanford.edu, cutkosky@stanford.edu
Documentation for asmeconf.cls: Version 1.45, December 25, 2025.

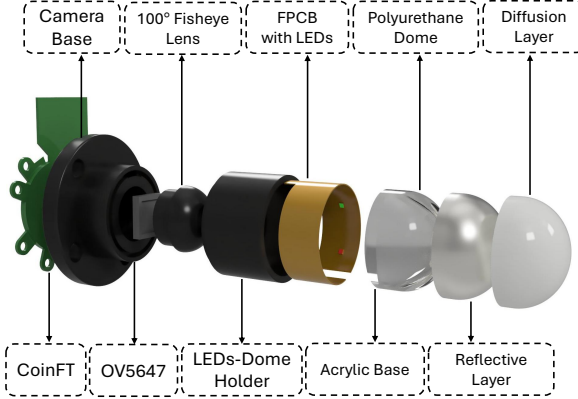


FIGURE 2: Exploded View of the PVFT multimodal sensing tool

force-torque sensor [15]. This design enables simultaneous acquisition of tactile deformations and dynamic force data under high loading conditions, suitable for subsurface feature detection and physiotherapy.

Using a Flexiv Rizon 4 robot, we performed controlled experiments with prepared tissue phantoms to detect tendon presence, diameter changes, depth variations, crossings, and tendon merging. Across all tasks, tactile imaging revealed clear geometric signatures, while force measurements provided complementary information for safe, stable, and clinically relevant interaction. Our main contributions are:

- PVFT, a compact multimodal tool for palpation and physiotherapy, capable of high-force deformation and contact force sensing.
- Phantom tissue experiments in which we demonstrate that tactile imaging resolves subsurface geometry that force alone cannot detect, while force/torque sensing provides contact force information, essential for controlled physical interaction.

Together, these results establish the utility of multimodal sensing for robotic palpation and physiotherapy, and lay the groundwork for future medical training, diagnostics, and autonomous therapeutic manipulation.

2. SENSOR FABRICATION AND CHARACTERIZATION

The PVFT sensor is constructed through a multi-stage fabrication process that integrates optical, mechanical, and force-sensing components (Fig. 2). The assembly consists of a fisheye imaging unit, an LED-illuminated dome, and a custom-designed 6-axis force–torque sensor.

2.1. Fabrication

A commercial camera (Arducam OV5647) is mounted onto a camera base, which ensures alignment between the imaging sensor and the dome’s optical center. A 100° fisheye lens is installed after removing the original lens from the camera, enabling coverage of the inner dome surface and minimizing distortion near the boundaries.

Illumination is provided by six RGB LEDs (NeoPixel Addressable 1515) soldered to a flexible PCB (FPCB). The LEDs are individually addressable and deliver high brightness with low heat generation, making them suitable for tactile imaging. The FPCB is inserted into a holder, printed using Markforged Onyx, a carbon-fiber-reinforced nylon composite as the camera base. The material choice provides high stiffness, low mass, and excellent dimensional stability, ensuring precise LED positioning and avoiding unwanted vibrations during robot motion. The matte-black surface finish reduces internal light reflections and improves image contrast.

The dome assembly is fabricated as a three-layer optical structure designed to remain robust under high contact loads while capturing deformation details. The primary polyurethane dome is cast using Smooth-On Clear Flex 30 in a mold, which provides a relatively stiff, optically clear shell with controlled wall thickness. This stiffness helps the dome reveal changes in contact patterns under large forces.

After curing, the outer surface of the dome is treated with a primer to activate the polyurethane and promote adhesion. A reflective layer is applied using a mirror-effect spray (Rust-Oleum 301494), forming a thin, uniform coating that enhances diffuse reflections and increases sensitivity to local deformation.

To create the diffusion layer, Clear Flex 30 is mixed with 2.5 wt% white silicone pigment and poured over the reflective surface. After leveling and curing, this semi-opaque layer smooths illumination gradients, suppresses LED hotspots, and improves overall image contrast. Once the three-layer dome is fully cured, the entire dome assembly is glued onto the LED-dome holder using hot glue.

2.2. Characterization

After mounting the CoinFT sensor beneath the optical dome, we calibrate the PVFT system. To establish accurate force references, the assembled sensor is mounted onto a commercial F/T sensor (ATI Industrial Automation, Gamma) which provides ground-truth force and torque measurements under controlled loading conditions. This setup enables calibration of both the optical and mechanical components in a single pass.

TABLE 1: Tendon detection performance across input modalities

Modality	Precision	Recall	F1 Score
Image (ResNet-18)	1.00	1.00	1.00
Sensor (MLP)	0.64	1.00	0.78
Combined (Late Fusion)	1.00	0.97	0.98

In addition to force calibration with the ATI Gamma, we perform task-specific calibration for high-force interactions using a soft phantom. We employ a 5-layer multilayer perceptron (MLP) model trained with an MSE loss. The calibration procedures include finger-poking tests as well as sliding and rolling tests under pressure. In total, we collect 33434 (23404 for training, 6686 for testing, and 3344 for validation) data points, and the rich interaction set covers a diverse range of changes in the force–torque (FT) data. All tests are conducted using a Flexiv Rizon 4 robot, which supports force control through an impedance control scheme.

3. PHANTOM EXPERIMENTS

3.1. Phantom preparation

Phantoms were prepared to simulate soft tissue with embedded tendons. The phantom material is cast Smooth-On Ecoflex 00-20 silicone. The tendons are 3D printed from PLA with Young's Modulus of 2.58 GPa, and experience some elastic deformation as one presses on the silicone above them. Prior to each set of tests we treated the upper surface of the phantom with mineral oil to reduce friction.

3.2. Test procedure

As illustrated in Figure 3, all experiments follow the same five-step protocol. We use the numeric labels (1–5) here and in subsequent plots to indicate the steps: (1) descent-to-force, (2) and (4) holding intervals, (3) lateral “ploughing” motion (sliding while maintaining high force that depresses the phantom tissue), and (5) final retraction.

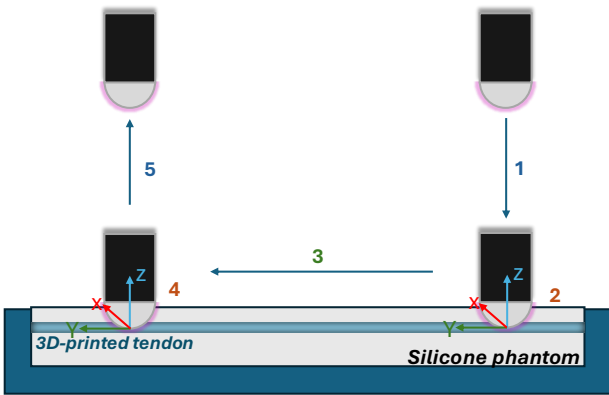


FIGURE 3: Procedure: (1) The robot descends along Z direction until the normal force reaches 25 N, 35 N or 45 N depending on the trial; (2) end-effector holds position for 1 s; (3) robot translates 120 mm along the +Y direction under position control; (4) a second 1 s holding phase; 5) the end-effector retracts and disengages.

Figure 4 shows a representative example with steps denoted using the same five labels. Dwell steps (2) and (4) are highlighted with light red shading. Note that between (2) and (4) some variation in force may occur, despite the constant Z position, due to buildup of forces and/or viscoelastic relaxation of the phantom material.

To quantify how the normal force changes during high-pressure sliding (“ploughing”), we define a force benchmark F_{bench} as the mean normal force measured during the first holding phase (region 2). The relative change of the normal force is computed as

$$\Delta F_z^{\text{rel}}(t) = \frac{F_z(t) - F_{\text{bench}}}{F_{\text{bench}}}. \quad (1)$$

This metric captures how much the instantaneous normal force deviates from the calibrated reference level. In Fig. 4b and similar plots, the shaded blue region represents the magnitude

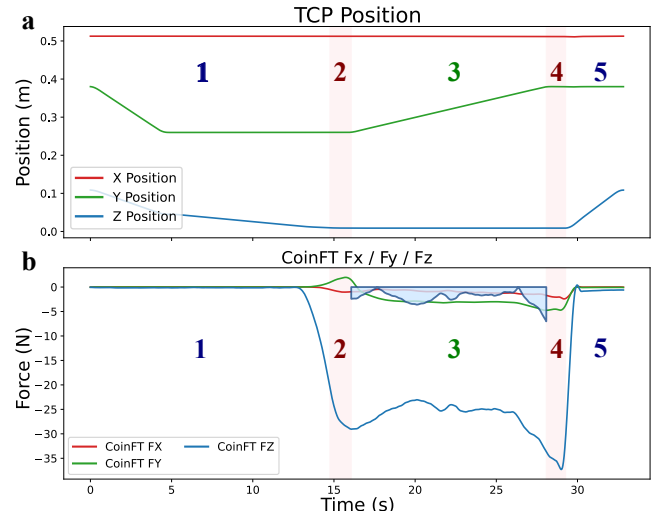


FIGURE 4: Typical motion (a) and force (b) plots corresponding to Fig. 3, in this case with a single uniform tendon along the whole length. The robot descends (1) until it reaches 25 N normal force. It then dwells (2) for 1 s and proceeds in the +Y direction (3) at constant Z height. Due to “ploughing” of the surface, there is some variation in F_z . The robot stops at (4) and departs in (5). Shaded blue region during step (3) shows the change in normal force per equation 2.

of force fluctuations during ploughing, we compute the absolute deviation from the benchmark force,

$$\Delta F_z^{\text{abs}}(t) = |F_z(t) - F_{\text{bench}}|. \quad (2)$$

For clearer visualization in the plot, we display the negative of this value, $-\Delta F_z^{\text{abs}}$.

3.3. Experiment 1: Transition From Tendon to No-Tendon

Figure 5 shows the system response when transitioning from a tendon into a no-tendon region under a 25 N initial normal force. The tactile snapshots in (a) exhibit distinct deformation patterns over the tendon compared with the softer silicone region, reflecting the subsurface differences. The paired cross-section schematic in (b) shows where these tactile views were captured.

Panels (c–e) summarize the corresponding robot motion and force measurements. The tool tip trajectory remains consistent, indicating that observed force variations originate from subsurface material differences rather than motion artifacts. As shown in (d), F_z decreases substantially when the tool moves from the tendon region into the softer silicone region, due to reduced surface stiffness. The relative change plot in (e) quantifies this effect: the deviation from the benchmark force increases significantly when transitioning away from the tendon.

Together, these results confirm that the system can distinguish between stiff (tendon) and soft (no-tendon) regions both in tactile appearance and in force response.

3.4. Experiment 2: Tendon Height Variation

Figure 6 presents an experiment in which the tendon maintains the same width but its centerline height differs by 1.5 mm

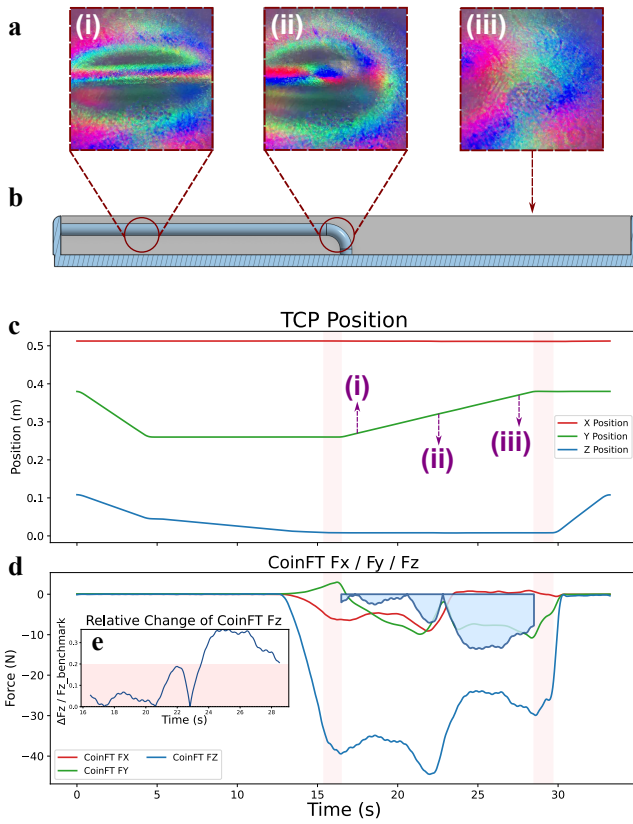


FIGURE 5: Multimodal sensing response when sliding from tendon to no-tendon regions. (a) Shows tactile images corresponding to regions noted in (b). Roman numerals (i), (ii), (iii) show the corresponding times in position (c) and force (d) plots. As in Fig. 4, shaded region shows $-\Delta F_z^{\text{abs}}$. Inset (e) shows normalized change in F_z during step 3.

between the left and right sides, connected by a sloped transition. Because this geometric variation is shallow, the normal-force response remains relatively unchanged. As shown in (d), the F_z signal exhibits only small fluctuations, insufficient to reliably indicate the depth change. In contrast, the tactile views in (a) reveal differences. The region with greater tendon height produces a more pronounced and elongated deformation pattern, while the lower region results in a flatter and more diffused signature. These differences arise from variations in silicone thickness and local dome conformity, making the tactile modality more sensitive than force in this scenario.

3.5. Experiment 3: Crossing vs. Straight Tendon Geometry

Figure 7 shows an experiment, performed under a higher 45 N nominal normal force. The tendon geometry begins with a crossed structure and then transitions into a straight 3.5 mm cylindrical tendon. Tendon depth is 2.3 mm below the surface.

The tactile views in (a) clearly differentiate the two different regions, showing that details of subsurface geometry are perceivable. In contrast, the force profile in (d) shows little change across this transition. Similarly, the relative-change curve in (e) shows no distinctive signature associated with the crossing-to-straight transition.

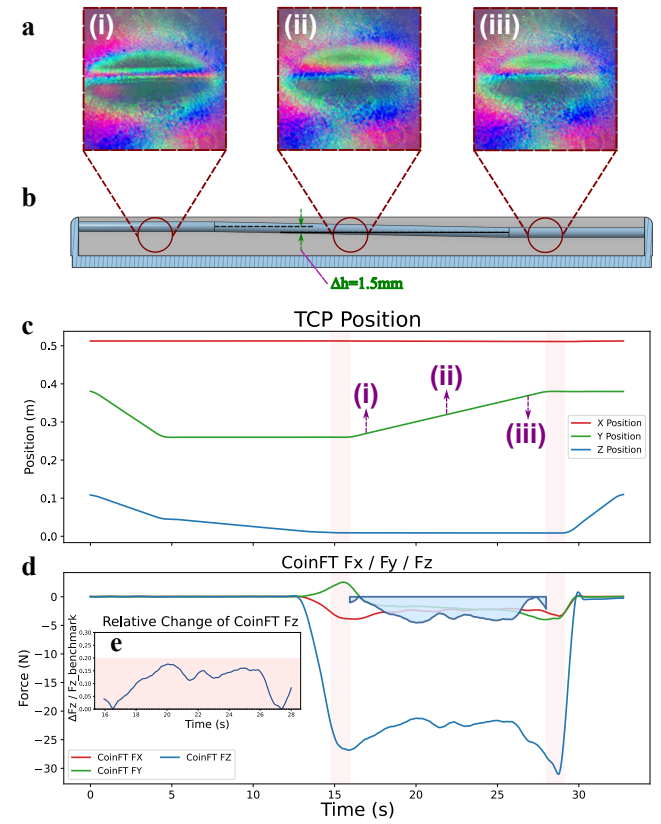


FIGURE 6: Multimodal sensing response to a shallow tendon-height variation ($\Delta h = 1.5$ mm). Labels follow the same convention as in Fig. 5.

3.6. Experiment 4: Distinguishing Tendon Multiplicity

Figure 8 presents an experiment in which the tendon geometry transitions from two thin parallel tendons into a single thicker tendon, all sharing the same top height, 1.8 mm below the surface. The top-view geometry shown in (b) highlights the lateral structural differences while keeping the vertical height constant.

The tactile snapshots in (a) clearly distinguish these regions: the two-tendon section produces a split, double-ridge deformation pattern, whereas the single thick tendon generates a broader, more unified footprint. In contrast, the force measurements in (d) show no stable or interpretable pattern across this transition. The F_z signal fluctuates due to soft-tissue deformation and robot-surface interaction but does not correlate reliably with the number of tendons beneath the sliding dome. The relative change plot in (e) similarly shows variations that are not correlated with the geometry shift. This confirms that force sensing alone is insufficient for detecting lateral structural differences when height and stiffness remain comparable.

Overall, this experiment demonstrates that tactile imaging is essential for identifying how many tendons are present and how they merge, while force signals remain ambiguous for this class of geometric transitions.

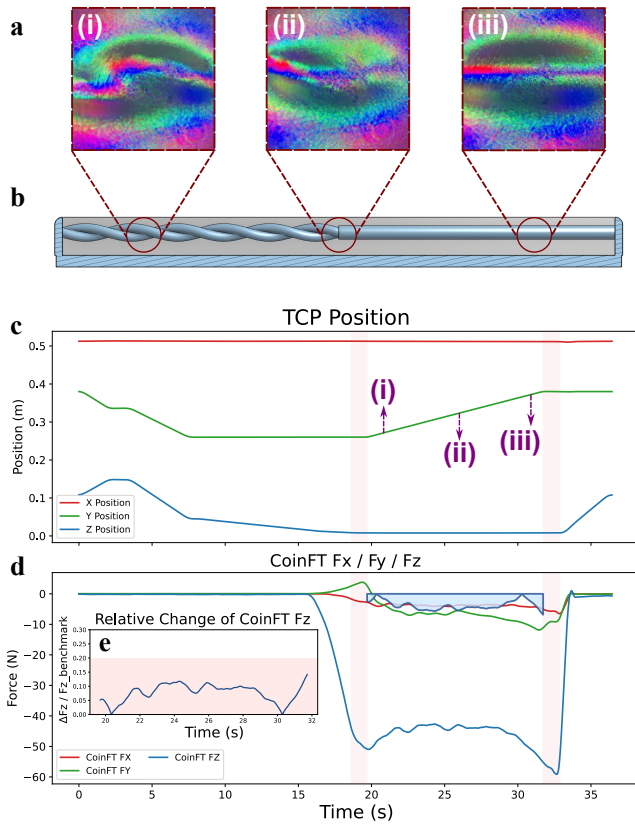


FIGURE 7: Multimodal sensing response when transitioning from a crossed tendon structure to a straight cylindrical tendon. Labels follow the same convention as in Fig. 5.

3.7. Force Control for Safe Tissue Interaction

Figure 9 shows an experiment for evaluating the role of force tracking from an application perspective. In physical-therapy tasks, maintaining a consistent therapeutic load is important for both treatment quality and patient safety. Here the CoinFT force/torque sensor is particularly useful, as it provides contact force data at 300 Hz.

We command a -25 N normal force and use CoinFT to provide data to command a consistent force using an impedance control scheme built into the Flexiv Rizon controller. The main plot shows that the measured force remains relatively consistent. However, there is gradual increase in the magnitude of F_z as the ploughing effects of pushing across the soft material start to rotate the tool and introduce relatively large bending moments at the CoinFT sensor, which fall outside the range of calibrated forces and moments. The inset quantifies this effect with a percentage error RMSE of 7.04%, indicating stable and reliable force tracking.

4. CONCLUSION

Across all experiments, our results demonstrate the advantages of combining tactile imaging with force sensing for characterizing subsurface biological structures and supporting physical-therapy interactions. While tactile images provide rich, spatially resolved information about local deformation patterns—revealing

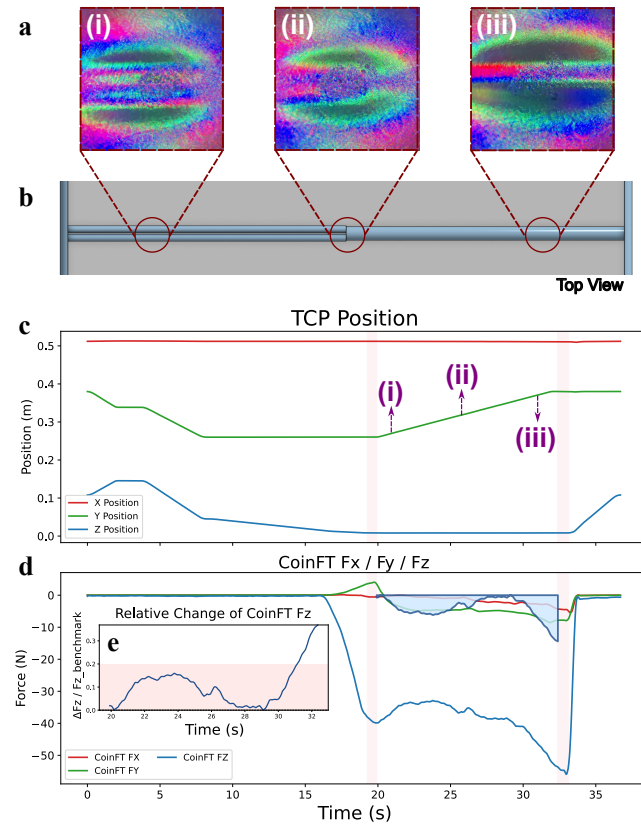


FIGURE 8: Multimodal sensing response when transitioning from two thin tendons to one thick tendon. Labels follow the same convention as in Fig. 5.

tendon presence, diameter changes, depth variations, crossings, and multiplicity—normal contact force alone often fails to capture these distinctions. In several experiments, even pronounced differences in tendon geometry produced subtle or inconsistent force signatures.

Our observations show that force responses are inherently difficult to predict, even under controlled conditions; qualitatively different experiment cases produced comparable variations in force. In comparison, tactile images revealed clear differences, with qualitatively different images corresponding to difference changes in conditions. Nonetheless, we argue that force sensing is valuable as it directly captures therapeutic pressure levels and

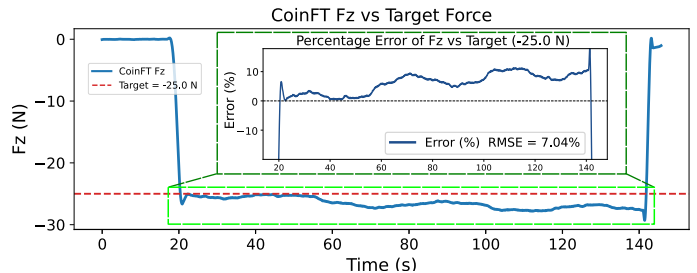


FIGURE 9: CoinFT normal-force tracking performance when maintaining a commanded 25 N load.

variations, and provides a basis for force control during sliding and rolling.

4.0.1. Future work: Building on these results, we plan to extend PVFT into a multimodal robot-learning framework that integrates tactile imaging, force feedback, and visual observations from the robot. By collecting demonstrations from expert clinicians and leveraging learning-based policy models such as diffusion policies, the robot could learn closed-loop palpation and treatment strategies that adapt to tendon geometry, depth, and orientation while maintaining safe therapeutic force levels. In parallel, we aim to exploit the rich tactile images and force signals for learning to infer subsurface structures directly from sensor data, enabling automatic tendon localization and characterization. Together, these directions represent a step toward safer, more repeatable, and more informative robot-assisted palpation and physiotherapy workflows.

ACKNOWLEDGMENTS

This work originated during Tian-Ao Ren's summer 2025 internship at Symbiokinetics Inc. We thank the Stanford Robotics Center for financial support during the summer term. We thank Symbiokinetics team for their collaboration and support throughout this project. We thank Stanley Wang and Venny Kojouharov for their help during the experimental work, and Mingyan Zhang for her help with figure preparation.

REFERENCES

- [1] Johansson, Roland S and Westling, Goran. "Roles of glabrous skin receptors and sensorimotor memory in automatic control of precision grip when lifting rougher or more slippery objects." *Experimental brain research* Vol. 56 No. 3 (1984): pp. 550–564.
- [2] Myburgh, Corrie, Larsen, Anders Holsgaard and Hartvigsen, Jan. "A systematic, critical review of manual palpation for identifying myofascial trigger points: evidence and clinical significance." *Archives of physical medicine and rehabilitation* Vol. 89 No. 6 (2008): pp. 1169–1176.
- [3] Zhang, Yingxuan, Ju, Feng, Wei, Xiaoyong, Wang, Dan and Wang, Yaoyao. "A piezoelectric tactile sensor for tissue stiffness detection with arbitrary contact angle." *Sensors* Vol. 20 No. 22 (2020): p. 6607.
- [4] Gwilliam, James C, Mahvash, Mohsen, Vagvolgyi, Balazs, Vacharat, Alexander, Yuh, David D and Okamura, Allison M. "Effects of haptic and graphical force feedback on teleoperated palpation." *2009 IEEE international conference on robotics and automation*: pp. 677–682. 2009. IEEE.
- [5] Harada, Naoya and Tasaki, Ryosuke. "Muscle knot state measurement using multi-axis kneading reaction force in physical massage robot system." *SICE Journal of Control, Measurement, and System Integration* (2025): pp. 1–9.
- [6] Xu, Wenjun, Guo, Jing and Ren, Hongliang. "Human palpation behavior modeling with mixture models: towards autonomous robotic palpation." *2018 3rd International Conference on Advanced Robotics and Mechatronics (ICARM)*: pp. 756–761. 2018. IEEE.
- [7] Konstantinova, Jelizaveta, Cotugno, Giuseppe, Dasgupta, Prokar, Althoefer, Kaspar and Nanayakkara, Thrishantha. "Autonomous robotic palpation of soft tissue using the modulation of applied force." *2016 6th IEEE International Conference on Biomedical Robotics and Biomechatronics (BioRob)*: pp. 323–328. 2016. IEEE.
- [8] Guo, Jing, Xiao, Bo and Ren, Hongliang. "Compensating uncertainties in force sensing for robotic-assisted palpation." *Applied Sciences* Vol. 9 No. 12 (2019): p. 2573.
- [9] Yuan, Wenzhen, Dong, Siyuan and Adelson, Edward H. "Gelsight: High-resolution robot tactile sensors for estimating geometry and force." *Sensors* Vol. 17 No. 12 (2017): p. 2762.
- [10] Lambeta, Mike, Chou, Po-Wei, Tian, Stephen, Yang, Brian, Maloon, Benjamin, Most, Victoria Rose, Stroud, Dave, Santos, Raymond, Byagowi, Ahmad, Kammerer, Gregg et al. "Digit: A novel design for a low-cost compact high-resolution tactile sensor with application to in-hand manipulation." *IEEE Robotics and Automation Letters* Vol. 5 No. 3 (2020): pp. 3838–3845.
- [11] Di, Julia, Dugonjic, Zdravko, Fu, Will, Wu, Tingfan, Mercado, Romeo, Sawyer, Kevin, Most, Victoria Rose, Kammerer, Gregg, Speidel, Stefanie, Fan, Richard E et al. "Using fiber optic bundles to miniaturize vision-based tactile sensors." *IEEE Transactions on Robotics* (2024).
- [12] Do, Won Kyung and Kennedy, Monroe. "Densetact: Optical tactile sensor for dense shape reconstruction." *2022 International Conference on Robotics and Automation (ICRA)*: pp. 6188–6194. 2022. IEEE.
- [13] Do, Won Kyung, Dhawan, Ankush Kundan, Kitzmann, Mathilda and Kennedy, Monroe. "Densetact-mini: an optical tactile sensor for grasping multi-scale objects from flat surfaces." *2024 IEEE international conference on robotics and automation (ICRA)*: pp. 6928–6934. 2024. IEEE.
- [14] Lambeta, Mike, Wu, Tingfan, Sengul, Ali, Most, Victoria Rose, Black, Nolan, Sawyer, Kevin, Mercado, Romeo, Qi, Haozhi, Sohn, Alexander, Taylor, Byron et al. "Digitizing touch with an artificial multimodal fingertip." *arXiv preprint arXiv:2411.02479* (2024).
- [15] Choi, Hojung, Low, Jun En, Huh, Tae Myung, Uribe, Gabriela A, Hong, Seongheon, Hoffman, Kenneth AW, Di, Julia, Chen, Tony G, Stanley, Andrew A and Cutkosky, Mark R. "Coinft: A coin-sized, capacitive 6-axis force torque sensor for robotic applications." *arXiv preprint arXiv:2503.19225* (2025).